Journal of Materials Chemistry C

ROYAL SOCIETY OF CHEMISTRY

COMMUNICATION

View Article Online
View Journal | View Issue

Check for updates

Cite this: *J. Mater. Chem. C*, 2021, **9**, 1555

Received 28th September 2020,
Accepted 14th December 2020

DOI: 10.1039/d0tc04625f

rsc.li/materials-c

Engineering Sr-doping for enabling long-term stable $FAPb_{1-x}Sr_xI_3$ quantum dots with 100% photoluminescence quantum yield†

Andrés F. Gualdrón-Reyes, *[a] David F. Macias-Pinilla, [a] Sofia Masi, [a] Carlos Echeverría-Arrondo, [a] Said Agouram, [bc] Vicente Muñoz-Sanjosé, [bc] Jhonatan Rodríguez-Pereira, [d] Jan M. Macak [de] and Iván Mora-Seró *[ac]

The Pb substitution in quantum dots (PQDs) with lesser toxic metals has been widely searched to be environmentally friendly, and be of comparable or improved performance compared to the lead-perovskite. However, the chemical nature of the lead substitute influences the incorporation mechanism into PQDs, which has not been explored in depth. In this work, we analyzed Sr-doping-induced changes in $FAPbI_3$ perovskites by studying the optical, structural properties and chemical environment of $FAPb_{1-x}Sr_xI_3$ PQDs. The substitution of Pb by 7 at% Sr allows us to achieve $FAPb_{1-x}Sr_xI_3$ PQDs with 100% PLQY, high stability for 8 months under a relative humidity of 40–50%, and T_{80} = 6.5 months, one of the highest values reported for halide PQDs under air ambient conditions. $FAPb_{0.93}Sr_{0.07}I_3$ PQDs also exhibit photobrightening under UV illumination for 12 h, recovering 100% PLQY at 15 days after synthesis. The suppression of structural defects mediated by Sr-doping decreases the non-radiative recombination mechanism. By attempting to increase the Sr content in PQDs, a mixture of 2D nanoplatelets/3D nanocubes has emerged, caused by a high Pb deficiency during the $FAPb_{1-x}Sr_xI_3$ synthesis. This contribution gives a novel insight to understand how the suitable/poor Pb substitution achieved through Sr-doping dictates the photophysical properties of PQDs that may be potentially applicable in optoelectronics.

1 Introduction

Considering the outstanding optoelectronic properties of different materials, it is unavoidable to refer halide perovskites, taking into account the research carried out in the last decade. The main features, such as the long diffusion length, strong sunlight harvesting and improved photocarrier mobility have led to the fabrication of efficient perovskite solar cells (PSCs) with the highest photoconversion efficiency at around 25.2% achieved until now.[1] In terms of competitiveness, PSCs have surpassed laboratory efficiencies of well-established technologies, such as polycrystalline Si, CIGS and CdTe solar devices.[1,2] However, PSCs suffer two main drawbacks: (i) the relatively low long-term stability reported for 3D halide perovskites based on $APbI_3$ (A = cesium, Cs^+; methylammonium, MA^+ and formamidinium, FA^+)[3–6] and (ii) the presence of toxic Pb. Moreover, the maximum theoretical performance from a 3D lead halide perovskite obtained with the black perovskite α-phase of $FAPbI_3$ stands at an efficiency of 32.3%, which is very close to the theoretical Schottky–Queisser limit.[7] Nevertheless, while α-$MAPbI_3$ is degraded under soft thermal conditions,[8] $CsPbI_3$ and $FAPbI_3$, which present higher long term stability, stabilize into a non-photoactive crystalline yellow δ-phase at room temperature.[3,6,9,10] Nonetheless, the stability of the black $FAPbI_3$ phase can be enhanced by the appropriate use of the surface energy.[10] To this extent, the synthesis of nanoconfined materials such as quantum dots can maintain the photoactive black phase structure and ensure the intrinsic optical properties.[10,11] Perovskite quantum dots (PQDs) also exhibit a tolerant-to-defect structure,[12] very high photoluminescence quantum yield (PLQY),[13] multiple exciton generation and a tunable band gap (E_g) through the composition engineering

[a] *Institute of Advanced Materials (INAM), Universitat Jaume I (UJI), Avenida de Vicent Sos Baynat, s/n, 12071 Castelló de la Plana, Castellón, Spain*
E-mail: sero@uji.es, gualdron@uji.es
[b] *Department of Applied Physics and Electromagnetism, University of Valencia, 46100 Valencia, Spain*
[c] *Materials for Renewable Energy (MAER), Unitat Mixta d'Investigació UV-UJI, 46010 Valencia, Spain*
[d] *Center of Materials and Nanotechnologies, Faculty of Chemical Technology, University of Pardubice, Nam. Cs. Legii 565, 53002 Pardubice, Czech Republic*
[e] *Central European Institute of Technology, Brno University of Technology, Purkyňova 123, 612 00 Brno, Czech Republic*

† Electronic supplementary information (ESI) available: Experimental setup, histograms, photoimages, SAED measurements, UV-Vis, PL, and XPS spectra, PL decays and tables of the optical properties, surface chemical composition, carrier lifetime and PLQY of the $FAPb_{1-x}Sr_xI_3$ PQDs colloidal solutions and redispersed precipitates. Excel file with the raw data of PLQY measurements. See DOI: 10.1039/d0tc04625f

or quantum confinement effect.[14–16] These features have allowed the facile processing and manufacturing of PQD colloidal solutions, fabricating highly efficient LEDs with external quantum efficiencies higher than 20%.[17] PQDs also show a good dot-to-dot electron transport ability,[18] providing a long electron lifetime.[19,20] Therefore, PQD solar cells have reached a certified record PCE of 16.6%, retaining 94% photoconversion after 600 h, using black-stabilized $Cs_{1-x}FA_xPbI_3$ PQDs.[19]

Although PQD-based devices could be available in future industrialization, the abovementioned toxic Pb is still a main concern to practical applications. In this context, the synthesis of less-toxic PQDs has been implemented through the metal replacement or doping[21] with different cations, such as Mn^{2+},[22] Zn^{2+},[23] Sb^{3+},[24] Sn^{2+},[25–27] or Ge^{2+}.[25,28–31] Sn and Ge are prone to oxidizing to their corresponding tetravalents Sn^{4+} and Ge^{4+} forms, respectively. This causes the formation of metal (M) vacancies in the perovskite structure, and deviations in the M–I octahedra connectivity, which in turn, decrease the defect tolerance and consequently the performance.[32] In the case of other elements, in general, the doping with new metals resulted in: (i) the suppression of a high density of non-radiative recombination pathways, increasing the photoluminescence quantum yield (PLQY) and providing suitable optoelectronic properties for LED fabrication,[23] and (ii) the stabilization of the photoactive black α-phase by reducing the PQDs size, due to the smaller ionic radius of the metal substitutes [for instance, Zn^{2+} (0.74 Å), Mn^{2+} (0.83 Å) Sb^{3+} (0.92 Å) and Sn^{2+} (0.93 Å)] compared with Pb^{2+} (1.19 Å).[23–25,33] Specifically, in the case of Zn^{2+}-modification, a maximum PLQY of around 98.5% is achieved after adding 36 at% Zn^{2+} into the $CsPbI_3$ structure. Here, alloyed $CsPb_{1-x}Zn_xI_3$ PQDs are generated, indicating that a large amount of the cation is introduced to improve the intrinsic properties of the host.[23] Therefore, a more recent strategy to substitute Pb emerges with the Sr^{2+} doping. This non-toxic divalent cation shows an identical ionic radius (1.18 Å) to that of Pb^{2+},[34] meeting all of the main characteristics for a total ion replacement, keeping the intrinsic properties of the host. By incorporating a Sr^{2+} content between 3–5 at% into the $CsPbI_3$ PQDs, the black phase stability is prolonged to around 2 months, improving the PLQY up to 95%.[35] At the doping level, this improvement surpasses the PLQY provided by the $CsPb_{1-x}Zn_xI_3$ PQDs (x up to 12 at%) around 60–70%.[23] In this context, Sr^{2+} is a promising dopant for enhancing the photophysical properties of iodide PQDs. However, even though the total Pb substitution could be accessible to synthesize $ASrI_3$, DFT calculations predict a wider band gap in these materials than those of the $APbI_3$ counterparts (3.6 eV for the case of $MASrI_3$).[36] These works point out that the chemical mechanisms that control the Pb replacement in PQDs are not fully understood.

In this work, we track the Sr-doping-induced photophysical properties in red-emitting $FAPb_{1-x}Sr_xI_3$ PQDs by varying the Sr fraction during their synthesis. The 7 at% Sr-doping provided $FAPb_{1-x}Sr_xI_3$ PQDs with 100% PLQY, which is higher and more stable than that for pure $FAPbI_3$, keeping a PLQY as high as 72% for 8 months after preparation. We concluded that Sr-doping maximized the suppression of the non-radiative recombination mechanism by reducing the density of the structural defects. For a higher Sr fraction, we evidenced the simultaneous emergence of 2D nanoplatelets, as the result of altering the stoichiometry of the precursors by a poor compensation of the Pb deficiency by Sr. According to these findings, the chemical nature and the content of lead substitute impacts on the synthesis of high-quality PQDs with desired photophysical properties. Furthermore, a mechanism for the Pb substitution controlled by Sr-doping can be established.

2 Analysis and discussion

The synthesis of the $FAPbI_3$ and $FAPb_{1-x}Sr_xI_3$ PQDs was carried out by varying the precursor Sr fraction. The procedure is the same for each concentration, keeping the total metal amount the same by properly changing the Pb : Sr ratio (see Experimental section). The final Sr fraction incorporated into the synthesized $FAPb_{1-x}Sr_xI_3$ PQDs has been determined by Energy-dispersive X-ray spectroscopy (EDS) to be 4, 7, 12 and 6 at%, corresponding to a nominal precursor composition of 30, 50, 60 and 70 at%, respectively, see Table 1. Samples were named, $FAPb_{1-x}Sr_xI_3$, considering x as the measured EDS composition, if nothing else is commented. Consequently, the amount of Sr incorporated into the PQD is significantly lower than the precursor ratio. The fact that the estimated Sr fraction is in the doping-range of 1–10 at%, compared with the nominal value, is strong evidence of the tough Pb substitution into the PQDs by Sr. A nanocube shape of the PQDs is evidenced for all the compositions, as shown in Fig. 1a–e, with an average particle size from 15 to 8.4 nm as a function of the nominal Sr content, in which higher Sr-doping entailed lower particle size. The size distribution for each composition is shown in Fig. S1a–e (ESI†). On the other hand, we determined the characteristic interplanar spacing of the analyzed PQDs as 0.64, 0.32, 0.29 and 0.23 nm (Fig. S2a–e, ESI†) through selected area electron diffraction (SAED). These values correspond to the (100), (200) (210) and (220) planes of the perovskite cubic crystal phase,[37,38] which are in good agreement with the XRD patterns obtained for the PQDs (Fig. 2). Previous reports in the literature have suggested that the reduction of the PQDs size at a higher fraction of metal halide is caused by the high consumption of iodide ions from the mixture reaction used for their stabilization.[23,35,39]

Table 1 Chemical composition of the as-prepared $FAPb_{1-x}Sr_xI_3$ PQD solutions, including the nominal and measured composition in the synthesized nanoparticles by EDS

Nominal composition	Nominal (x) [Sr/(Sr + Pb)]	Percentage of elements calculated by EDS			Calculated (x) [Sr/(Sr + Pb)]	Calculated I/(Pb + Sr) ratio
		I	Pb	Sr		
$FAPbI_3$	—	74.9	25.1	—	—	2.98
x = 0.3	0.3	76.3	22.6	1.1	0.04	3.22
x = 0.5	0.5	79.0	19.5	1.5	0.07	3.76
x = 0.6	0.6	73.7	23.0	3.3	0.12	2.80
x = 0.7	0.7	73.6	24.9	1.5	0.06	2.78

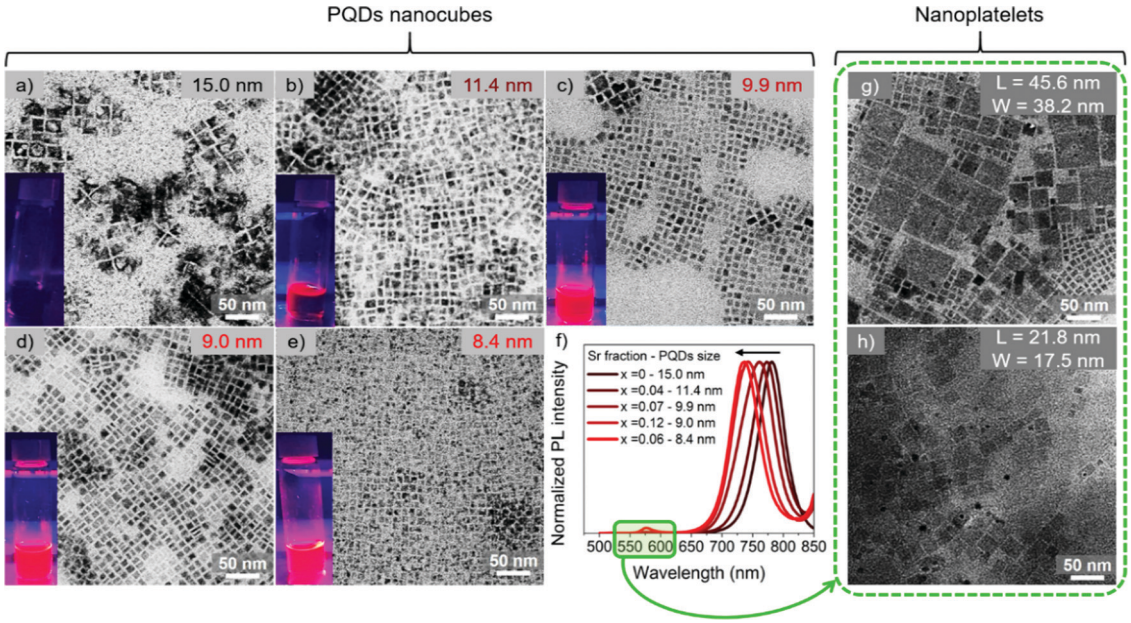

Fig. 1 TEM images of (a) $FAPbI_3$ and $FAPb_{1-x}Sr_xI_3$ perovskite quantum dot (PQDs) colloidal solutions with (b) 4 at%, Sr, (c) 7 at% Sr, (d) 12 at% Sr, and (e) 6 at% Sr. (f) Photoluminescence (PL) spectra of the $FAPb_{1-x}Sr_xI_3$ PQD colloidal solutions by varying the Sr fraction-particle size. TEM images of the (g) $FAPb_{0.88}Sr_{0.12}I_3$ and (h) $FAPb_{0.94}Sr_{0.06}I_3$ nanoplatelets (NPLs) from the redispersed precipitate by varying their corresponding lateral dimensions (L = length, W = width).

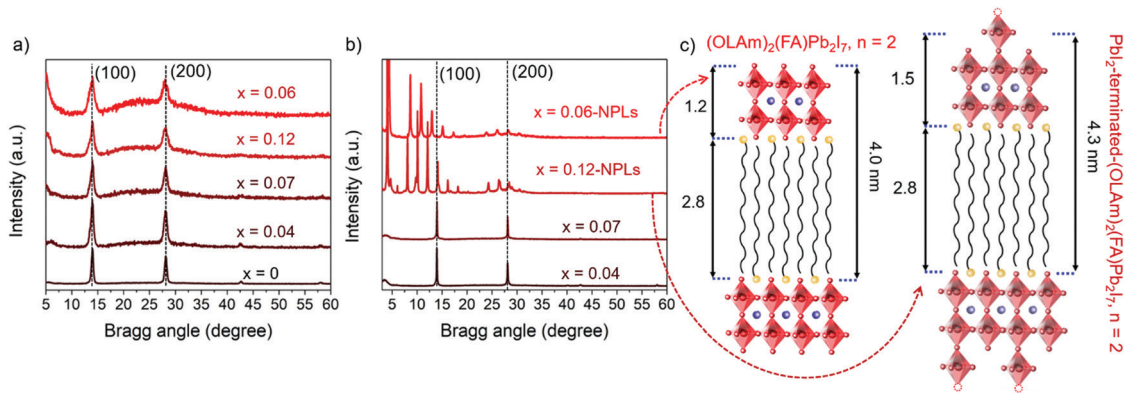

Fig. 2 XRD patterns of the (a) $FAPb_{1-x}Sr_xI_3$ PQDs colloidal solutions, and (b) their corresponding redispersed precipitates. (c) Schematic representations of the layered perovskite spacings and relevant distances for $FAPb_{0.88}Sr_{0.12}I_3$ and $FAPb_{0.94}Sr_{0.06}I_3$ NPLs.

To give a clear understanding about the role of iodide anions on the PQDs growth and stabilization, we consider some characteristics from the surface chemistry of PQDs. First, the high surface-to-volume ratio of small PQDs generates a substantial density of halide vacancies on their surface (undercoordinated Pb).[40] These structural defects are quickly passivated by the available halide ions from the mixture reaction. Simultaneously, oleylammonium (OLAm) cations bounded to halides can substitute and fill some A-cation positions into the cuboctahedral place of perovskite,[41] compensating the negative charge and decreasing the surface energy.[40] The replacement of a high fraction of A-cation sites by the long alkylammonium chain is known as instant capping, and restricts the PQDs dimensions.[41] This phenomenon justifies the formation of stable $FAPb_{1-x}Sr_xI_3$ PQDs with smaller size since the OLA/Pb molar ratio increases as the Pb content decreases (Pb deficiency) by Sr addition (see Table 2). According to this depiction, we suggest that the synthesis of stabilized PQDs requires the use of both SrI_2 and PbI_2 to keep a high iodide fraction in the mixture reaction to reduce defect formation, even though the Pb deficiency is not fully compensated by Sr incorporation, as we analyze below. To verify this hypothesis, we attempted to grow $FAPb_{0.93}Sr_{0.07}I_3$ PQDs in the absence of the nominal amount of SrI_2 added in the mixture reaction, keeping the amount of PbI_2 unchanged (Fig. S3, ESI†). As expected, we were not able to synthesize the desired material. Therefore, we assume that the amount of iodide anions in the mixture reaction is constant, and the I/Pb molar ratio increases with the amount of nominal Sr (see Table 2).

Table 2 Summary of the calculation of OLA/Pb, I/Pb molar ratios and the Pb deficiency in the synthesis of $FAPb_{1-x}Sr_xI_3$ perovskite quantum dots

Nominal composition	Calculated composition/ doping, EDS	Amount of added PbI_2[a]|SrI_2 (Pb^{2+}|Sr^{2+}) in the synthesis (mmol)	OLA[b]/ Pb molar ratio	I^-[c]/Pb molar ratio
$FAPbI_3$	$FAPbI_3$	0.74 | 0	12.32	2
$x = 0.3$	$x = 0.04$	0.52 | 0.22	17.53	2.84
$x = 0.5$	$x = 0.07$	0.37 | 0.37	24.64	4
$x = 0.6$	$x = 0.12$	0.30 | 0.44	30.40	4.93
$x = 0.7$	$x = 0.06$	0.22 | 0.52	41.45	6.73

[a] Amount of PbI_2 (Pb^{2+}) in the synthesis. [b] Amount of OLA into the synthesis (mmol): 9.12. [c] Amount of I^- into the synthesis (mmol): 1.48.

The change in size is correlated with a change in the optical properties of $FAPb_{1-x}Sr_xI_3$ PQDs colloidal solutions. Sr-doping blueshifts the photoluminescence (PL) emission of pure $FAPbI_3$ progressively, as shown in Fig. 1f and the inset pictures in Fig. 1a–e. This behavior is also reflected in the absorbance spectra of $FAPb_{1-x}Sr_xI_3$, as shown in Fig. S1f (ESI†). The corresponding optical features of the PQDs are summarized in Table S1 (ESI†). It should be noted that Sr-doping induced a smaller particle size than the Bohr diameter of $FAPbI_3$ ($\sim$ 12.7 nm).[42] Consequently, a blueshift is expected due to the quantum confinement effect.[23,35] Moreover, two more emission peaks/absorption edges were observed at lower wavelengths at around 511–524 nm and 567–577 nm, respectively, as shown in Fig. S4 (ESI†), when the Sr-doping level surpassed 7 at%. The existence of new PL emission signals suggested the co-existence of diverse structures in the dispersion. To give a suitable explanation for this observation, we first examined the appearance of both PQD colloidal solutions and precipitate materials, which was simultaneously obtained for each $FAPb_{1-x}Sr_xI_3$ material after the synthesis. It was noted that a precipitate appeared after the PQD synthesis. Precipitates from the $FAPb_{0.96}Sr_{0.04}I_3$ and $FAPb_{0.93}Sr_{0.07}I_3$ syntheses exhibited the same dark coloration as the precipitate from the $FAPbI_3$ synthesis, while precipitates from $FAPb_{0.88}Sr_{0.12}I_3$ and $FAPb_{0.94}Sr_{0.06}I_3$ were more reddish than their corresponding colloidal solutions. Precipitates were separated from the colloidal solutions and redispersed in hexane, as shown in Fig. S5a (ESI†), for further analysis. By conducting TEM images on the $FAPb_{0.88}Sr_{0.12}I_3$ and $FAPb_{0.94}Sr_{0.06}I_3$ precipitates, we were able to find evidence of a mixture of nanoparticle morphology of both nanoplatelets (NPLs) and PQDs nanocubes, as shown in Fig. 1g and h. The predominance of the 2D structure over the 3D one is clear. The dimensions of the $FAPb_{0.88}Sr_{0.12}I_3$ ($FAPb_{0.94}Sr_{0.06}I_3$) NPLs are 45.6 (21.8) nm length, and 38.2 (17.5) nm width, respectively. The distribution of the dimensions for these two materials are displayed in Fig. S5b, c and S5b′, c′ (ESI†), respectively. Additionally, the UV-Vis and PL features of the bare $FAPb_{0.88}Sr_{0.12}I_3$ ($FAPb_{0.94}Sr_{0.06}I_3$) precipitates (Fig. S5d and e, ESI†) exhibit absorption edges/emission peaks centered at 589 (590) nm and 583 (586) and at 530 nm, respectively, pointing out that the origin of the extra peaks in the PQDs colloidal solution comes from the NPLs. This evidence is in accordance with the layered-2D Ruddlesden–Popper structures, showing formula $(LA)_2(A)_{n-1}Pb_nI_{3n+1}$, $n = 1$ and $n = 2$, where A = FA^+ and LA is referred to a long alkylammonium chain, and n is the number of the layers of octahedra in the perovskite-like stack, as reported in the literature[43–46] For our case, OLAm is the capping ligand occupying the LA positions in the 2D perovskites. At this stage, we deduced that the incorporation of 7 at% Sr (nominal precursor ratio of 0.5, see Table 1) is the maximum Sr-doping that promotes the synthesis of just PQDs without altering their shape and optical properties. By surpassing this nominal Sr precursor ratio of 0.5, the PQDs synthesis is altered, causing the emergence of 2D NPLs.

As shown in Fig. 2a, the $FAPbI_3$ and $FAPb_{1-x}Sr_xI_3$ PQDs extracted from the colloidal solutions present two main peaks at 14° and 28°, respectively. These signals are associated with the (100) and (200) planes of a typical perovskite lattice $FAPbI_3$ crystallizing in the simple cubic black phase (PDF 54-0752).[14,37] Moreover, after Sr-doping, the XRD peaks do not exhibit any shift,[34,47,48] which is supportive of the non-detected lattice distortion.[34] However, the $FAPb_{1-x}Sr_xI_3$ PQDs XRD peaks suffer a clear broadening, which can be associated with the PQD size decrease, although an inhomogeneous strain or microstrain cannot be ruled out.[34] The low Sr fraction incorporated into the $FAPbI_3$ PQDs structure preserved the crystal structure until a doping level of 7 at%. Sr was achieved. Phung *et al.*[34] revealed that the Sr-$MAPbI_3$ bulk films can incorporate up to 0.2 at% Sr, promoting Sr^{2+} segregation to the perovskite surface at a higher content. We believe that the presence of a higher Sr fraction into the PQDs than the estimated one in bulk films can be attributed to the facile dissolution of the Sr-precursor by the presence of capping ligands, releasing more Sr^{2+} cations during the synthesis to occupy Pb^{2+} positions. Thus, the emergence of the 2D structures is related to the different processability of Sr- and Pb-precursors to define the PQDs growth. The cubic phase is preserved in the PQDs by introducing Sr up to 7 at%, as shown in Fig. 2b, while well-defined peaks at low angles appear in the XRD profiles of the redispersed precipitates, for a nominal Sr precursor ratio higher than 0.5, confirming the NPL crystalline nature observed by TEM.[43,49]

To determinate the number of layers contained in the NPLs, the n value from the Ruddlesden–Popper structures was calculated. The XRD peaks of each sample follow periodic small angle intervals, associated with nanoplatelet stacking.[43,50] The diffraction peaks of $FAPb_{0.88}Sr_{0.12}I_3$ and $FAPb_{0.94}Sr_{0.06}I_3$ NPLs display a regular 2θ increment of around 2.04° and 2.25°, respectively, as shown in Fig. S6 (ESI†). By using the Bragg equation, the periodic spacing (d) forming these periodicities is estimated to be around 4.3 nm and 4.0 nm, respectively. As shown in Fig. 2c, these values are associated with the distance between the $[PbX_6]^{4-}$ octahedra layers, separated by OLAm cations.[43,50] Consequently, the thickness of the inorganic framework, excluding the long organic chains of the OLAm, of the $FAPb_{0.88}Sr_{0.12}I_3$ and $FAPb_{0.94}Sr_{0.06}I_3$ NPLs is calculated as 1.5 nm and 1.2 nm thick, respectively. The $FAPb_{0.94}Sr_{0.06}I_3$ NPLs structure is the same as that for the Ruddlesden–Popper $(OLAm)_2(FA)Pb_2I_7$ perovskite ($n = 2$),[49,51] even if we do not discard the mixture of 2D structures with different "n", since the optical features of the colloidal solutions and precipitates at least suggest the formation of two

layered structures (n = 1, n = 2). Regarding the $FAPb_{0.88}Sr_{0.12}I_3$ NPLs, the disparity in thickness compared with the benchmark value for a double metal halide octahedra layer (1.2 nm),[51] matches well with the presence of undercoordinated Pb positions in the form of distorted $[PbI_5]^{3-}$ units on the NPLs surface, as shown in Fig. 2c. In this context, the $FAPb_{0.88}Sr_{0.12}I_3$ NPLs present a PbI_2-terminated-$(OLAm)_2(FA)Pb_2I_7$ structure (n = 2). Thus, the co-existence of 2D/3D structures is the result of the poor compensation of Pb positions by Sr into PQDs, associated with structural defects, like undercoordinated Pb.

The increase of the nominal Sr precursor fraction significantly impacts the chemical environment of $FAPb_{1-x}Sr_xI_3$, as it has been analyzed by X-ray photoelectron spectroscopy (XPS) (Fig. S7a and b, ESI†). It has identified the existence of C, N, O, Pb and I in PQDs and NPLs, while the presence of Sr is detected only in the PQDs. The corresponding chemical composition of PQDs and NPLs are summarized in Tables S2 and S3 (ESI†), respectively. In the high resolution (HR) XPS Sr $3p_{3/2}$ spectra of $FAPb_{1-x}Sr_xI_3$ PQDs, as shown in Fig. S7c and d (ESI†), a weak and noisy signal was attained. This response is ascribed to the presence of substitutional Sr^{2+} in the perovskite structure,[34,52] replacing Pb^{2+}. The low signal-to-noise ratio, the difference in intensity, and the absence of the main signal of substitutional Sr^{2+} in the Sr $3p_{3/2}$ spectra of some samples points to an inhomogeneity of Sr incorporation into PQDs.[52] On the other hand, Fig. 3a and b show the HR-XPS Pb 4f spectra obtained for PQDs and NPLs, where the main $Pb4f_{7/2}$ and $Pb4f_{5/2}$ peaks are decomposed into two doublets. The first one is located at 138/143 eV, associated with the presence of Pb^{2+} from the perovskite lattice, while the second doublet at 136/141 eV corresponds to metallic lead, Pb^0. The existence of Pb^0 is closely related with the presence of iodide vacancies in the materials.[14] According to the low complexation affinity between Pb^{2+} and I^-, and the dynamic nature of the capping ligands on the PQDs surface, iodide loss can be facilitated,[53] leaving undercoordinated Pb or releasing Pb^0 to the surface. This fact provides a more defective material.[14] Therefore, in a Pb-deficient iodide perovskite, halide defects are formed with the concomitant generation of Pb^{2+} vacancies.[34] The absence of one neighboring Pb^{2+} causes the formation of two I^- vacancies in order to keep the electroneutrality in the perovskite lattice, creating Schottky defects.[34,54] Thus, it is expected that more Schottky defects (higher Pb^0 fraction) are formed by intensifying the Pb deficiency, as the amount of Pb precursor is decreased in the PQD synthesis. However, our findings show that incorporated Sr (Fig. 3c) can decrease the Pb^{2+} vacancies, and consequently, the defect density in PQDs under certain circumstances.

A good parameter to evaluate the fraction of defects is the metallic lead-to-total metal ratio denoted as $Pb^0/(Sr + Pb_{total})$ (see Table S2, ESI† and Fig. 3d). This parameter has been calculated in order to analyze the Sr-doping-induced variation of the Pb-/iodide-vacancies fraction contained in the $FAPb_{1-x}Sr_xI_3$ PQDs. As seen in Fig. 3d, the lowest $Pb^0/(Sr + Pb_{total})$ ratio is obtained for $FAPb_{0.93}Sr_{0.07}I_3$ PQDs (see Table S2, ESI†). In this case, the incorporation of Sr^{2+} maximizes the reduction of Pb^0, and consequently reduces the formation of Pb^{2+} vacancies and Schottky defects.

Regarding iodine, its corresponding HR-XPS spectra exhibit the I 3d doublet centered at 619/631 eV, as shown in Fig. S8a and b (ESI†). This doublet is attributed to the presence of iodide anions from the $[PbI_6]$ octahedra that make up the PQDs and NPLs structure.[14] Even though the amount of Pb decreases due to the Sr incorporation, as shown in Table 2, the addition of stoichiometric amounts of PbI_2 and SrI_2 to the reaction mixture allows us to assume that the iodide fraction is kept constant. In this context, a lower amount of iodide anions from the total available amount will react with a lesser amount of Pb to synthesize PQDs, increasing the amount of free iodide anions.

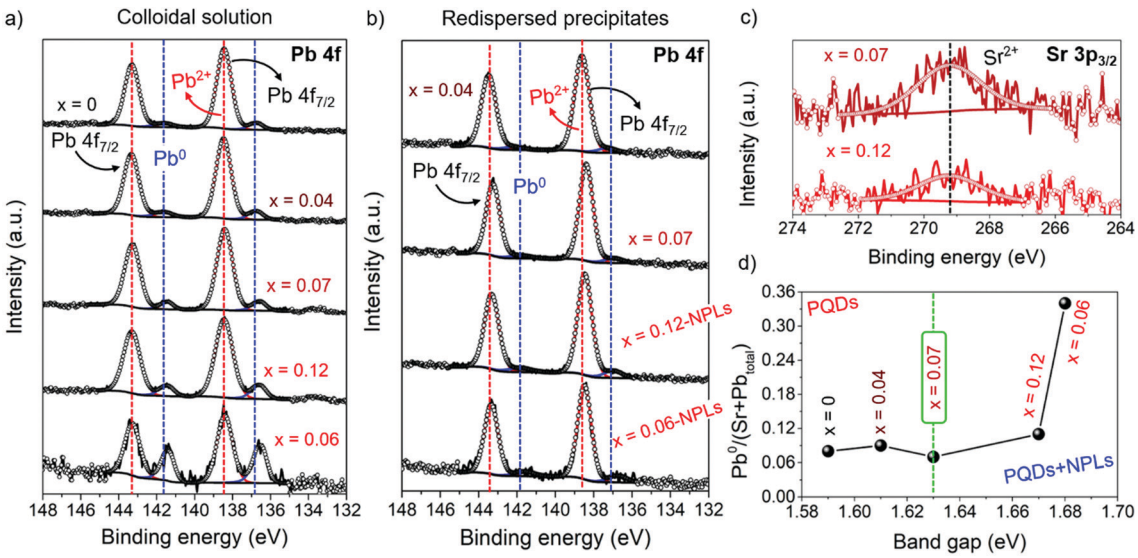

Fig. 3 High-resolution (HR) XPS spectra of (a and b) Pb 4f, (c) XPS Sr $3p_{3/2}$ and (d) calculated metallic Pb-to-$(Sr + Pb_{total})$ ratio for (a, c and d) $FAPb_{1-x}Sr_xI_3$ PQDs colloidal solutions, and (b) their corresponding redispersed precipitates.

This is the source of iodide needed to support the Schottky defect reduction, facilitating the Sr^{2+}-doping. This fact can also explain the rise of the I/(Pb + Sr) ratio determined in the $FAPb_{1-x}Sr_xI_3$ colloidal solutions through EDS (Table 1), and the gradual increase of the I/Pb^{2+} atomic ratio in the surface chemical atomic composition of these materials, as shown in Table S2 (ESI†), to reach the maximum point for the $FAPb_{0.93}Sr_{0.07}I_3$ PQDs. However, when the Pb deficiency is intensified after adding a large amount of Sr precursor to the mixture reaction, there is not enough available iodide species (as it has been employed in the formation of NPLs, see below) to restrain the formation of Schottky defects (see Table S2 (ESI†), Fig. 3d). Consequently, a lower Sr fraction is incorporated to replace the Pb^{2+} positions, as we can observe in Table 1.

The existence of Schottky defects induced by the distribution of free iodide anions can be also corroborated through the rise of Pb^0 density estimated for the $FAPb_{1-x}Sr_xI_3$ redispersed samples with x = 0.12 and x = 0.06 (Table S3, ESI†). Without a doubt, the distribution of building blocks to obtain both PQDs and NPLs does not satisfy their own chemical composition, contributing to the growth of high-defective perovskites. The Sr-doping is also appreciated in the shift of the Pb^0 doublets, as shown in Fig. 3a, from the $FAPb_{1-x}Sr_xI_3$ PQDs to the lower binding energies (BEs), as a result of the lower electronegativity of Sr compared with Pb.[34] On the other hand, by attempting to introduce a higher Sr fraction to reduce the Pb fraction, the $Pb^0/(Sr + Pb_{total})$ markedly increases. Hence, we can claim that the incorporation of 7 at% Sr into the $FAPb_{1-x}Sr_xI_3$ PQDs generates a suitable compensation of Pb deficiency, preserving the PQDs structure and producing less-defective materials.

These results also show the problem of using Sr to substitute Pb in higher ratios, despite their similarities, as the Sr incorporation in PQDs is significantly below that of the precursor ratio. According to these features, Sr-doping is preferred instead of the total Pb replacement. Differences in the chemistry of the two metals justify the difficulty of Sr incorporation, as shown in the sketch in Fig. 4a. First of all, PbI_2 is known to crystallize in a rhombohedral structure,[36] where the distorted PbI_6 octahedra are face-sharing one another into layers connected by weak van der Waals forces. In the presence of OA and OLA in stoichiometric amounts, two simultaneous reactions happen: PbI_2 rapidly dissolves with OA to produce hydroiodic acid (HI); then, this strong acid reacts with OLA, yielding the OLAm-I species in the mixture reaction (reactions 1 and 2):[55,56]

$$PbI2(sol) + xC_{18}COOH_{(l)} \rightarrow (C_{18}COO)_xPbI_{2-x(sol)} + HI_{(sol)} \quad x = 1 \text{ or } 2 \quad (1)$$

$$xC_{18}NH_{2(l)} + xHI_{(sol)}C_{18}NH_{3(sol)}{}^{+} + xI_{(sol)}{}^{-} \quad x = 1 \text{ or } 2 \quad (2)$$

A suitable amount of OLAm-I is now available to be intercalated into the lead octahedra frameworks, transforming from

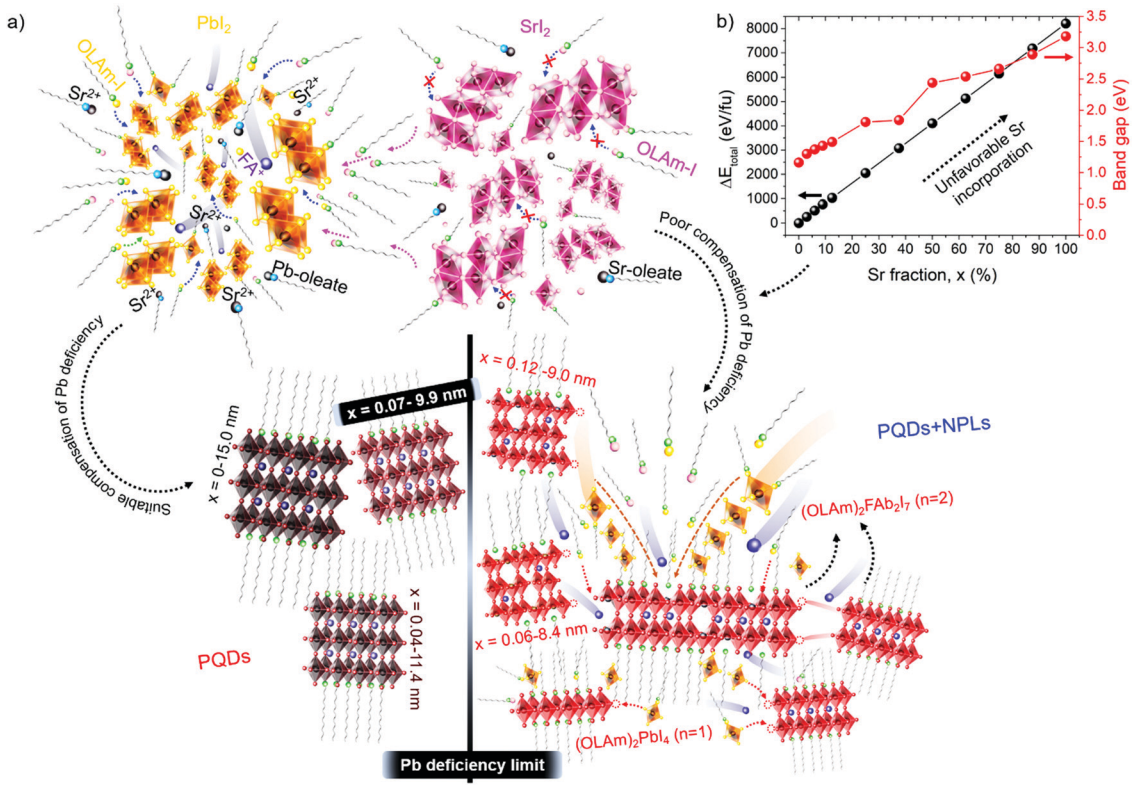

Fig. 4 (a) Schematic representation of the emergence of PQDs and NPLs caused by the Pb deficiency. A suitable Sr fraction compensating Pb positions provides Sr-modified nanocubes with a low density of structural defects. The poor compensation of Pb deficiency by Sr produces a mixture of defective 2D/3D structures. (b) DFT total energy of bulk cubic $FAPb_{1-x}Sr_xI_3$ as a function of the Sr fraction and corresponding band gap, where "fu" in the y-axis refers to formula unit.

a face-sharing to a corner-sharing structure. Then, the coordinated PbI_3^- structures are achieved (reaction 3):[55]

$$PbI_{2(sol)} + C_{18}NH_3^+I_{(sol)}^- \rightarrow C_{18}NH_3^+PbI_{3(sol)}^- \quad (3)$$

The coordinated PbI_3^- react with FA^+ cations during hot-injection to provide the $FAPbI_3$ structure.

Lastly, the combination of OA and OLA into the mixture reaction produces oleylammonium oleate (reaction 4).[57,58] This species is ionically coordinated to the PQDs surface, providing the material stabilization.

$$C_{18}NH_{2(l)} + C_{18}COOH_{(l)} \rightleftharpoons C_{18}NH_{3(sol)}^+ + C_{18}COO_{(sol)}^- \quad (4)$$

Unlike the Pb precursor, SrI_2 shows an orthorhombic crystal lattice, where Sr is coordinated to 7 iodine atoms, and prefers the formation of a $[SrI_7]^{5-}$ pentagonal bipyramidal structure.[36] This system does not present a face-sharing structure as PbI_2, but each bipyramidal unit is interconnected to each other. Based on the low Sr fraction found in the $FAPb_{1-x}Sr_xI_3$ PQDs, we propose that the availability of Sr^{2+} cations to dope the PQDs is promoted by the dissolution of some bipyramidal units of SrI_2 in the presence OLA and OA, similar to PbI_2 (reactions 5 and 6):

$$SrI2(sol) + yC_{18}COOH_{(l)} \rightarrow (C_{18}COO)_ySrI_{2-y(sol)} + HI_{(sol)} \quad y = 1 \text{ or } 2 \quad (5)$$

$$yC_{18}NH_{2(l)} + yHI_{(sol)}C_{18}NH_{3(sol)}^+ + yI_{(sol)}^- \quad y = 1 \text{ or } 2 \quad (6)$$

Nevertheless, the poor compensation of the Pb deficiency by Sr incorporation allows us to deduce that the OLAm-I product formed in reaction 6 is not able to modify the interconnected $[SrI_7]^{5-}$ bipyramidal units, unlike PbI_2, restraining the reaction with FA^+ cations. This fact can explain why it is necessary to add a high Sr-precursor content in the mixture reaction to reach the Sr^{2+}-doping level, as we detected by EDS. On the other hand, the non-incorporated Sr^{2+} can also react with oleate anions to produce Sr-oleate in the mixture reaction. However, attending to reactions 1, 2, 5 and 6, Sr-oleate can be formed without altering the acid–base balance and the subsequent formation of the $OLAm^+$ cations.

To understand the difficulty of the Sr incorporation, we have calculated by density functional theory (DFT) methods the total energy of cubic $FAPb_{1-x}Sr_xI_3$ in the bulk ($0 \leq x \leq 100\%$), as shown in Fig. 4b. It is apparent that small fractions of Pb up to 7% can be substituted by Sr atoms in the lattice without significantly altering the cubic symmetry of $FAPbI_3$. However, the total energy continuously increases with a higher Sr fraction, confirming the eventual destabilization of the cubic geometry.[35] The rise of the total energy was accompanied by a band gap broadening in agreement with the experimental trend, as shown in Table S1 (ESI†). Moreover, we have calculated the formation energies of the bulk compounds $FAPbI_3$ and $FASrI_3$ in the absence of defects. They are −0.072 Ry (−94.52 kJ mol^{-1}) and −0.069 Ry (−90.58 kJ mol^{-1}), respectively, and more details can be found in the ESI.† The smaller stability of the pure $FASrI_3$ perovskite is consistent with the proven difficulty to convert one compound into the other by Sr incorporation. These results prove that a greater reorganization of the SrI_2 structure is required to synthesize $FAPb_{1-x}Sr_xI_3$ PQDs with stoichiometric fractions of SrI_2 and PbI_2, which is not possible at least under our synthetic conditions. On the other hand, DFT also predicts that the incorporation of Sr produces a widening of the bandgap, as shown in Fig. 4b. This fact allows us to explain the observed blueshift in the PL emission, shown in Fig. 1f, despite the increase of the quantum confinement regime, shown in Fig. 1a–e.

Evidently, if the Pb deficiency is poorly compensated by Sr during synthesis, the Sr-doping-induced modification in the stoichiometry of the precursors determines the growth of different perovskite structures from 3D. In this scenario, the OLA/Pb molar ratio is increased, while the mixture reaction shows an iodide-rich environment (higher I/Pb molar ratio). Under this consideration, the formation of OLAm-I is accelerated to produce highly coordinated iodoplumbates species, schematized in reaction 7:[55]

$$PbI_{2(sol)} + xC_{18}NH_3^+I_{(sol)}^- \rightarrow (C_{18}NH_3^+)_x(PbI_{2+x})^{x-} \quad x \geq 2 \quad (7)$$

The number of $[PbI_4]^{2-}$ species counterbalanced with OLAm cations are the basic building blocks for establishing the structure of the layered 2D perovskites with formula $[(RNH_3)_2(PbI_4)]_n$.[55] On the other hand, the thickness of a 2D perovskite depends on the competition between the A-site cations, trying to expand the perovskite growth from the planar layer, and the alkylammonium cations attempting to compress the growth into the planar layer.[51] In our context, the small thickness of the obtained NPLs implies that a lower density of FA^+ cannot balance the effect of OLAm. In other words, a high density of the OLAm species would occupy the FA^+ positions, confining its thickness to two $[PbI_6]^{4-}$ layers (~1.2 nm). This argument can explain the concurrent formation of PQDs and NPLs in our samples, as a direct reflection that the fraction of FA^+ cations is distributed to stabilize both 2D and 3D structures. At the same time, the excess of OLAm-I needed to promote the NPLs growth according to the reaction 7 (higher coverage of OLAm/surface area, as shown in Table S4 (ESI†), can also mediate the growth of PQDs (reaction 3). This fact indicates that not only iodide vacancies are formed due to the free iodide distribution in both kinds of structures, generating consequently Schottky defects. Hence, if the free iodide fraction from the mixture reaction is consumed by the NPLs formation as a consequence of a marked Pb deficiency, it is expected that a lower Sr fraction can dope PQDs, reducing the likelihood to suppress Schottky defects. This would explain why, upon adding more Sr from 60 to 70 at% nominal Sr content, there is a decrease in the found Sr into PQDs from 12 to 6 at%, respectively. However, the co-existence of PQDs with NPLs indicates that there is enough OLM to stabilize both morphologies (higher OLA/Pb), facilitating the instant capping of PQDs, which is reflected in the smaller particle size observed by

TEM. At this stage, we concluded that the poor compensation of the Pb deficiency by Sr substitution lies in the difficulty to modify the crystal structure of the Sr precursor compared with its lead analogue during PQDs synthesis. This fact is the critical point to trigger the alteration in the stoichiometry of the precursors to favor the growth of defective PQDs and NPLs.

Moreover, it has been established that the halide vacancies are the Achilles' heel of perovskite stability, providing a facile way for the oxygen incorporation and, in turn, causing its self-degradation.[14] After introducing a controlled amount of Sr into the $FAPbI_3$ PQDs, we significantly reduce the structural defects fraction. Thus, we could expect a Sr-doping-induced improvement in their long-term stability, and also of the optical properties in comparison with $FAPbI_3$ PQDs.

From this perspective, we studied the photoluminescence quantum yield (PLQY) for all of the $FAPb_{1-x}Sr_xI_3$ PQDs. It is worth noting that 100% PLQY corresponding to a Sr fraction of 7 at% was obtained, shown in Fig. 5a, associating this outstanding optical behavior to the maximum suppression of halide defects, shown in Fig. 3d. Here, the non-radiative carrier recombination channel is suppressed. However, when the Sr fraction is raised, the PLQY value rapidly decreased, as shown in Fig. 5a, indicating the appearance of non-radiative recombination channels. To get a closer look at the recombination kinetics of the PQDs samples, we carried out time-resolved PL measurements, as shown in Fig. S9 (ESI†), collecting their corresponding average electron lifetimes, τ_{avg}, by fitting the PL decays through a bi-exponential equation, $y = y_0 + A_1e^{-x/\tau_1} + A_2e^{-x/\tau_2}$. As seen in Fig. 5a, the higher the band gap of $FAPb_{1-x}Sr_xI_3$ PQDs, the lower the τ_{avg} (see the discussion below). An Excel file with the raw data of the PLQY measurements is included as ESI.†

Taking into account the PLQY, it is possible to determine the radiative (k_r) and non-radiative recombination (k_{nr}) decay rate constants (Table S5, ESI†).[59] Interestingly, k_{nr}, shown in Fig. 5b, shows a similar behavior to that of the $Pb^0/(Sr + Pb_{total})$ ratio estimated by XPS, shown in Fig. 3d, confirming that the suppression of iodide vacancies (Schottky defects) by adding Sr up to 7 at% into the $FAPb_{1-x}Sr_xI_3$ PQDs quenches the non-radiative channel. At this stage, we expected to obtain a single-exponential behavior to describe the longer PL decays. Nevertheless, a bi-exponential behavior depicts the PL dynamics better. The PL decay profile of 100% PLQYs does not exhibit single-exponential decay behavior, a fact that could be explained by the trapping detrapping-processes with shallow defects in the perovskite conduction band, as it has been previously reported.[60] Accordingly, we suggest that Sr modification also plays a main role in the recombination kinetics of PQDs. Yao *et al.* reported that Sr^{2+} can provide radiative energy levels near or into the conduction band (CB) states from $CsPbI_3$ QDs. Then, these states induce a radiative recombination, which is the key point to increasing the PLQY.[35]

According to this fact, Sr not only mitigates the formation of carrier traps provided by the existence of iodide vacancies, but also introduces radiative recombination sites, which can explain the formation of high-quality $FAPb_{1-x}Sr_xI_3$ PQDs with 100% PLQY. Nevertheless, the reduction of the PL lifetime is ascribed to the growth of smaller PQDs, a consequence of the poor compensation of Pb deficiency (instant capping). In this context, a stronger quantum confinement is achieved, increasing the exciton binding energy and making the carrier recombination faster. This trend has been also reported for PQDs with near-unity PLQY, where the metal-doping is chosen as an alternative to improve the photophysical properties of the perovskites.[23,35] On the other hand, the rapid raise of k_{nr}, as shown in Fig. 5b, at higher Sr fraction causes an increase of the k_{nr}/k_r rate, as shown in Fig. 5c. In this case, the difficult incorporation of Sr into the $FAPbI_3$ PQDs causes Sr to not completely compensate the higher Pb deficiency, and the use of free iodide anions from the mixture reaction in the formation of NPLs avoids the suppression of Schottky defects. According to the fact that these defects act like non-recombination sites for carriers, the PLQY of the PQDs is reduced.

The PLQY of the synthesized samples was followed for 30 days in the dark under ambient conditions, as shown in Fig. 6a, and exposed to a high relative ambient humidity between 40–50%. The PLQY values of the PQDs obtained during measurements as a function of time are summarized in Table S6 (ESI†). As shown in Fig. 6b, the PLQY of the $FAPb_{0.93}Sr_{0.07}I_3$ PQDs continuously decreases after being practically null after 15 days. However, for samples containing Sr, the PLQY stabilizes after 3–6 days, preserving a value as high as 78% $FAPb_{0.93}Sr_{0.07}I_3$ PQDs after 30 days. The stability of the different PQDs under continuous UV illumination has also

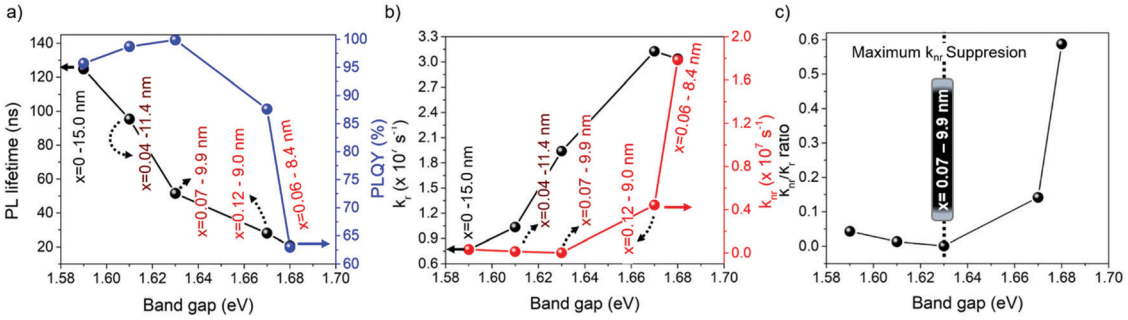

Fig. 5 (a) Behavior of the PL lifetime and PLQY, (b) radiative (k_r) and non-radiative recombination (k_{nr}) decay rate constants, and (c) their corresponding k_{nr}/k_r ratio for the $FAPb_{1-x}Sr_xI_3$ PQDs colloidal solutions by varying the Sr fraction.

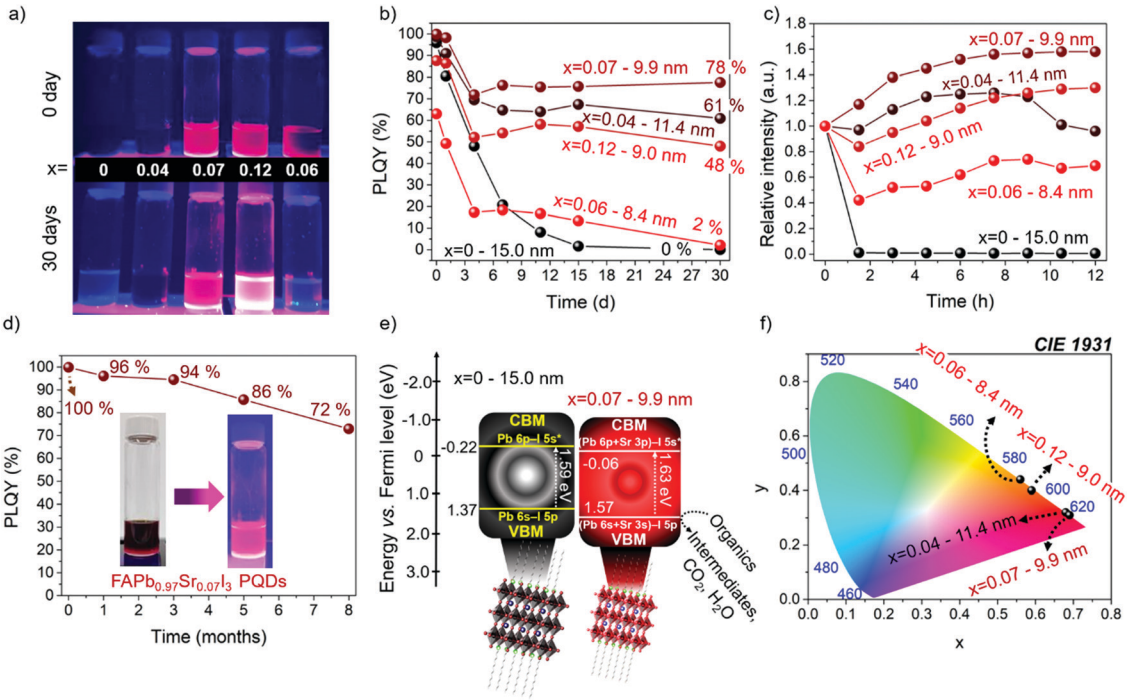

Fig. 6 (a) Photographs of fresh and aged (after 30 days) $FAPb_{1-x}Sr_xI_3$ PQDs colloidal solutions under UV-light irradiation. (b) PLQY values as a function of aged days for PQDs colloidal solutions. (c) Photostability of 15 days-aged PQDs exposed to UV light irradiation for 15 h. (d) PLQY stability of $FAPb_{0.93}Sr_{0.07}I_3$ PQDs colloidal solutions for 8 months, with T_{80} = 6.5 months. (e) Band structure of $FAPbI_3$ and $FAPb_{0.93}Sr_{0.07}I_3$ PQDs obtained from XPS VB spectra through the extrapolation method. (f) CIE chromaticity of Sr-substituted PQDs.

been analyzed, as shown in Fig. 6c. The PLQY of samples aged for 15 days at room conditions was tracked during 12 h under continuous UV illumination. We observed that the relative PL intensity increased for all Sr-modified PQDs, associated with a phenomenon known as photobrightening.[2] Although the reasons to describe this effect are still under debate, the passivation of halide defects by the presence of oxygen/superoxide anions has been considered as the most accepted explanation.[61] In this context, we suggest that the suppression of a high density of Schottky defects by the Sr inclusion facilitates the passivation of residual electron traps by oxygen species. Interestingly, $FAPb_{0.93}Sr_{0.07}I_3$ PQDs aged for 15 days recovered the 100% PLQY after UV illumination. Nonetheless, an excess of adsorbed oxygen also instigates the self-degradation of the perovskites, origin of the immediate PL quenching of $FAPbI_3$, and the hampered photobrightening of the $FAPb_{0.94}Sr_{0.06}I_3$ PQDs.

It is worth highlighting that $FAPb_{0.93}Sr_{0.07}I_3$ sample stored in the fridge (under dark conditions and 4 °C) is stable for at least 8 months preserving a significant PLQY of 72%, as shown in Fig. 6d and Table S7 (ESI†), with T_{80} = 6.5 months, where T_{80} is the time for which the initial PLQY is reduced by 20%. Accordingly, the red-emitting $FAPb_{1-x}Sr_xI_3$ PQDs synthetized in this work shows higher PLQY and stability than other modified FA-based iodide perovskite PQDs, such as $FAPb_{1-x}Sn_xI_3$, (PLQY = 63% for 2 months),[25] established red-emitting Zn- (PLQY = 98.5% for 2.3 months)[23] and Sr-doped $CsPbI_3$ PQDs (PLQY = 95% for 2 months),[35] and competitive optical properties comparable with the longest-term stable $FAPbI_3$ QDs reported until now: Ding *et al.*[38] (PLQY = 100% for 4 months), Protesescu *et al.*[45] (PLQY = 70% for 6 months).

Finally, to give clear insight into the potential application of the $FAPb_{1-x}Sr_xI_3$ PQDs, we estimated the band structure of the materials by XPS valence band spectrum in the presence and absence of Sr^{2+} energy levels. The valence band energy (E_{VB}) of the $FAPb_{0.93}Sr_{0.07}I_3$ PQDs is calculated by extrapolation method, as shown in Fig. S10 (ESI†), and then the associated CB energy (E_{CB}) is obtained through the equation $E_{VB} = E_{CB} + E_g$. By comparing with un-substituted $FAPbI_3$, the VB position of the Sr-substituted PQDs is displaced to more positive energy values (*vs.* Fermi level) (Fig. 6e). This Sr-doping-induced modification potentially boost the oxidizing power to $FAPb_{0.93}Sr_{0.07}I_3$ PQDs to carry out, for instance, the degradation of organics,[14] whether some reaction conditions (electrolyte, irradiation source/time and reaction medium) are well established. On the other hand, the downward shift of the relative position of CB of PQDs with the incorporation of Sr was also shifted to more positive values. This indicated that the presence of Sr^{2+} can suppress some electron traps near the CB, and favors the radiative recombination pathway, as shown in Fig. 5b. Moreover the CIE chromaticity coordinates (x,y) are calculated from the PL spectra of the $FAPb_{1-x}Sr_xI_3$ PQDs samples, as shown in Table S8 (ESI†). Interestingly, the chromaticity values of the $FAPb_{0.93}Sr_{0.07}I_3$ PQDs are close to the Rec. 2020 standards for the red color (0.708, 0.292)[62] (Fig. 6f). This fact allows us to deduce that the Sr-doping is suitable in this synthetic protocol to obtain PQDs with a purer color. Additionally, features such

as high PLQY and stability of the PQDs provide the potential to fabricate competitive red-emitting diodes.

3 Conclusions

In this work, we synthesized $FAPb_{1-x}Sr_xI_3$ PQDs by using the hot-injection method, with the purpose of enhancing their photophysical properties and extending the long-term stability of the PQDs. These facts that undoubtedly increase the interest of these systems for optoelectronic applications. We elucidated that the difficulty of Sr incorporation to replace Pb during the PQDs synthesis lies in the different crystalline structure of the Sr precursor compared with its Pb analogues, restraining the formation of building blocks for PQDs growth. Thus, metal doping in PQDs is carried out instead of total Pb substitution. In this context, just a relatively low amount of Sr (in the doping range of 4–12 at%) can be incorporated into the PQDs substituting Pb. In addition, the progressive substitution of Pb by Sr increases the total energy of the system, as we have calculated by DFT. This is an indication of the hindered Sr incorporation. We observe that for ratios of Sr/Pb precursors higher than 0.5, the synthesis produces not just quantum dots but also nanoplatelets. Interestingly, we observed that for ratios of Sr/Pb precursors lower than 0.5, both the Sr incorporation and the excess of I into the PQDs decrease the Pb- and I-vacancies to form Schottky defects. Additionally, the energy states provided by Sr-doping induce the radiative recombination into PQDs. Nevertheless, for ratios of Sr/Pb precursors higher than 0.5, the formation of nanoplatelets removes the excess I, and the density of Schottky defects increases. Thus, the Sr-doping-induced change in the optical properties and PQDs long-term stability have been unveiled. Under optimized conditions, $FAPb_{0.93}Sr_{0.07}I_3$ PQDs synthesized with a Sr/Pb precursor ratio of 0.5 eliminates the non-radiative recombination pathways reaching a 100% PLQY. The decrease of defects also improves the long-term stability of $FAPb_{1-x}Sr_xI_3$ PQDs. The $FAPb_{0.93}Sr_{0.07}I_3$ PQDs present a significant 72% PLQY after 8 months, with T_{80} = 6.5 months, one of the highest reported for halide perovskite quantum dots, owing to the fact that the PQDS were not stored under an inert atmosphere. $FAPb_{0.93}Sr_{0.07}I_3$ PQDs also exhibit photobrightening under UV illumination for 12 h, recovering the 100% PLQY after aging for 15 days. All of these results point to the significant Sr-doping-induced reduction of defects in the synthesized $FAPb_{0.93}Sr_{0.07}I_3$ PQDs. Consequently, the Sr-doping-induced outstanding photophysical properties makes the $FAPb_{1-x}Sr_xI_3$ PQDs excellent candidates to improve the performance of optoelectronic devices and to conduct lead solar driven processes more efficiently.

Author contributions

A. F. G.-R. and I. M.-S. conceived the project. A. F. G.-R., S. M. and I. M.-S. designed the experiments. A. F. G.-R. synthesized the PQDs and performed the corresponding optical properties. S. A. and V. M.-S. conducted the TEM and EDS measurements of the materials. J. R.-P. and J. M. M. contributed to the XPS measurements and analysis. D. F. M. P. and C. E. A. carried out the DFT calculations for energy formation. A. F. G.-R. coordinated the experimental work. D. F. M. P. and C. E. A. coordinated the theoretical work. I. M.-S. coordinated the whole project. A. F. G.-R., S. M. and I. M.-S. wrote the manuscript. All of the authors contributed to the discussions.

Conflicts of interest

The authors declare no competing interests.

Acknowledgements

This work was supported by the European Research Council (ERC) *via* Consolidator Grant (724424–No-LIMIT) and the European Commission *via* FET Open Grant (862656 – DROP-IT), EU (FEDER) and MINECO under project TEC2017-85912-C2-2, and Generalitat Valenciana *via* Prometeo Grant Q-Devices (Prometeo/2018/098). We acknowledge the SCSIE from the University of Valencia for providing TEM facilities. CEMNAT project LM2018103 funded by the Ministry of Youth, Education and Sports of the Czech Republic is acknowledged for the financial support of the XPS measurements. We acknowledge SCIC from Jaume I University (UJI) for help with the XRD characterization. We also acknowledge to Juan I. Climente for his assistance in the theoretical work.

References

1 M. A. Green, E. D. Dunlop, J. Hohl-Ebinger, M. Yoshita, N. Kopidakis and A. W. Y. Ho-Baillie, *Prog. Photovoltaics Res. Appl.*, 2020, **28**, 3–15.
2 Z. Andaji-Garmaroudi, M. Anaya, A. J. Pearson and S. D. Stranks, *Adv. Energy Mater.*, 2020, **10**, 1903109.
3 S. Masi, C. Echeverría-Arrondo, K. M. M. Salim, T. T. Ngo, P. F. Mendez, E. López-Fraguas, D. F. Macias-Pinilla, J. Planelles, J. I. Climente and I. Mora-Seró, *ACS Energy Lett.*, 2020, **5**, 418–427.
4 X. Zheng, C. Wu, S. K. Jha, Z. Li, K. Zhu and S. Priya, *ACS Energy Lett.*, 2016, **1**, 1014–1020.
5 J. A. Steele, H. Jin, I. Dovgaliuk, R. F. Berger, T. Braeckevelt, H. Yuan, C. Martin, E. Solano, K. Lejaeghere, S. M. J. Rogge, C. Notebaert, W. Vandezande, K. P. F. Janssen, B. Goderis, E. Debroye, Y.-K. Wang, Y. Dong, D. Ma, M. Saidaminov, H. Tan, Z. Lu, V. Dyadkin, D. Chernyshov, V. Van Speybroeck, E. H. Sargent, J. Hofkens and M. B. J. Roeffaers, *Science*, 2019, **365**, 679–684.
6 A. Marronnier, G. Roma, S. Boyer-Richard, L. Pedesseau, J.-M. Jancu, Y. Bonnassieux, C. Katan, C. C. Stoumpos, M. G. Kanatzidis and J. Even, *ACS Nano*, 2018, **12**, 3477–3486.
7 W. Shockley and H. J. Queisser, *J. Appl. Phys.*, 1961, **32**, 510–519.
8 S. Ma, S. H. Kim, B. Jeong, H.-C. Kwon, S.-C. Yun, G. Jang, H. Yang, C. Park, D. Lee and J. Moon, *Small*, 2019, **15**, 1900219.

9 Y. Fan, H. Meng, L. Wang and S. Pang, *Sol. RRL*, 2019, **3**, 1900215.
10 S. Masi, A. F. Gualdrón-Reyes and I. Mora-Seró, *ACS Energy Lett.*, 2020, 1974–1985, DOI: 10.1021/acsenergylett.0c00801.
11 J. Xue, J.-W. Lee, Z. Dai, R. Wang, S. Nuryyeva, M. E. Liao, S.-Y. Chang, L. Meng, D. Meng, P. Sun, O. Lin, M. S. Goorsky and Y. Yang, *Joule*, 2018, **2**, 1866–1878.
12 A. Swarnkar, V. K. Ravi and A. Nag, *ACS Energy Lett.*, 2017, **2**, 1089–1098.
13 L. Protesescu, S. Yakunin, M. I. Bodnarchuk, F. Krieg, R. Caputo, C. H. Hendon, R. X. Yang, A. Walsh and M. V. Kovalenko, *Nano Lett.*, 2015, **15**, 3692–3696.
14 A. F. Gualdrón-Reyes, J. Rodríguez-Pereira, E. Amado-González, J. Rueda-P, R. Ospina, S. Masi, S. J. Yoon, J. Tirado, F. Jaramillo, S. Agouram, V. Muñoz-Sanjosé, S. Giménez and I. Mora-Seró, *ACS Appl. Mater. Interfaces*, 2020, **12**, 914–924.
15 M. Suri, A. Hazarika, B. W. Larson, Q. Zhao, M. Vallés-Pelarda, T. D. Siegler, M. K. Abney, A. J. Ferguson, B. A. Korgel and J. M. Luther, *ACS Energy Lett.*, 2019, **4**, 1954–1960.
16 M. Que, Z. Dai, H. Yang, H. Zhu, Y. Zong, W. Que, N. P. Padture, Y. Zhou and O. Chen, *ACS Energy Lett.*, 2019, **4**, 1970–1975.
17 K. Lin, J. Xing, L. N. Quan, F. P. G. de Arquer, X. Gong, J. Lu, L. Xie, W. Zhao, D. Zhang, C. Yan, W. Li, X. Liu, Y. Lu, J. Kirman, E. H. Sargent, Q. Xiong and Z. Wei, *Nature*, 2018, **562**, 245–248.
18 Q. Zhao, A. Hazarika, X. Chen, S. P. Harvey, B. W. Larson, G. R. Teeter, J. Liu, T. Song, C. Xiao, L. Shaw, M. Zhang, G. Li, M. C. Beard and J. M. Luther, *Nat. Commun.*, 2019, **10**, 2842.
19 M. Hao, Y. Bai, S. Zeiske, L. Ren, J. Liu, Y. Yuan, N. Zarrabi, N. Cheng, M. Ghasemi, P. Chen, M. Lyu, D. He, J.-H. Yun, Y. Du, Y. Wang, S. Ding, A. Armin, P. Meredith, G. Liu, H.-M. Cheng and L. Wang, *Nat. Energy*, 2020, **5**, 79–88.
20 S. Seth, T. Ahmed, A. De and A. Samanta, *ACS Energy Lett.*, 2019, **4**, 1610–1618.
21 Y. Zhou, J. Chen, O. M. Bakr and H.-T. Sun, *Chem. Mater.*, 2018, **30**, 6589–6613.
22 Q. A. Akkerman, D. Meggiolaro, Z. Dang, F. De Angelis and L. Manna, *ACS Energy Lett.*, 2017, **2**, 2183–2186.
23 X. Shen, Y. Zhang, S. V. Kershaw, T. Li, C. Wang, X. Zhang, W. Wang, D. Li, Y. Wang, M. Lu, L. Zhang, C. Sun, D. Zhao, G. Qin, X. Bai, W. W. Yu and A. L. Rogach, *Nano Lett.*, 2019, **19**, 1552–1559.
24 S. Bera, D. Ghosh, A. Dutta, S. Bhattacharyya, S. Chakraborty and N. Pradhan, *ACS Energy Lett.*, 2019, **4**, 1364–1369.
25 R. Begum, X. Y. Chin, M. Li, B. Damodaran, T. C. Sum, S. Mhaisalkar and N. Mathews, *Chem. Commun.*, 2019, **55**, 5451–5454.
26 F. Liu, C. Ding, Y. Zhang, T. S. Ripolles, T. Kamisaka, T. Toyoda, S. Hayase, T. Minemoto, K. Yoshino, S. Dai, M. Yanagida, H. Noguchi and Q. Shen, *J. Am. Chem. Soc.*, 2017, **139**, 16708–16719.
27 A. B. F. Vitoreti, S. Agouram, M. Solis de la Fuente, V. Muñoz-Sanjosé, M. A. Schiavon and I. Mora-Seró, *J. Phys. Chem. C*, 2018, **122**, 14222–14231.
28 X. Wu, W. Song, Q. Li, X. Zhao, D. He and Z. Quan, *Chem. – Asian J.*, 2018, **13**, 1654–1659.
29 F. Liu, C. Ding, Y. Zhang, T. Kamisaka, Q. Zhao, J. M. Luther, T. Toyoda, S. Hayase, T. Minemoto, K. Yoshino, B. Zhang, S. Dai, J. Jiang, S. Tao and Q. Shen, *Chem. Mater.*, 2019, **31**, 798–807.
30 Y. Wang, J. Tu, T. Li, C. Tao, X. Deng and Z. Li, *J. Mater. Chem. A*, 2019, **7**, 7683–7690.
31 F. Liu, Y. Zhang, C. Ding, K. Kawabata, Y. Yoshihara, T. Toyoda, S. Hayase, T. Minemoto, R. Wang and Q. Shen, *Chem. Mater.*, 2020, **32**, 1089–1100.
32 S. Khalfin and Y. Bekenstein, *Nanoscale*, 2019, **11**, 8665–8679.
33 S. Zhou, Y. Zhu, J. Zhong, F. Tian, H. Huang, J. Chen and D. Chen, *Nanoscale*, 2019, **11**, 12465–12470.
34 N. Phung, R. Félix, D. Meggiolaro, A. Al-Ashouri, G. Sousa e Silva, C. Hartmann, J. Hidalgo, H. Köbler, E. Mosconi, B. Lai, R. Gunder, M. Li, K.-L. Wang, Z.-K. Wang, K. Nie, E. Handick, R. G. Wilks, J. A. Marquez, B. Rech, T. Unold, J.-P. Correa-Baena, S. Albrecht, F. D. Angelis, M. Bär and A. Abate, *J. Am. Chem. Soc.*, 2020, **142**, 2364–2374.
35 J.-S. Yao, J. Ge, K.-H. Wang, G. Zhang, B.-S. Zhu, C. Chen, Q. Zhang, Y. Luo, S.-H. Yu and H.-B. Yao, *J. Am. Chem. Soc.*, 2019, **141**, 2069–2079.
36 T. J. Jacobsson, M. Pazoki, A. Hagfeldt and T. Edvinsson, *J. Phys. Chem. C*, 2015, **119**, 25673–25683.
37 L.-Q. Xie, L. Chen, Z.-A. Nan, H.-X. Lin, T. Wang, D.-P. Zhan, J.-W. Yan, B.-W. Mao and Z.-Q. Tian, *J. Am. Chem. Soc.*, 2017, **139**, 3320–3323.
38 C. Ding, F. Liu, Y. Zhang, D. Hirotani, X. Rin, S. Hayase, T. Minemoto, T. Masuda, R. Wang and Q. Shen, *Nano Energy*, 2020, **67**, 104267.
39 Y. Dong, T. Qiao, D. Kim, D. Parobek, D. Rossi and D. H. Son, *Nano Lett.*, 2018, **18**, 3716–3722.
40 Y. Fu, T. Wu, J. Wang, J. Zhai, M. J. Shearer, Y. Zhao, R. J. Hamers, E. Kan, K. Deng, X. Y. Zhu and S. Jin, *Nano Lett.*, 2017, **17**, 4405–4414.
41 A. Dutta, S. K. Dutta, S. D. Adhikari and N. Pradhan, *ACS Energy Lett.*, 2018, **3**, 329–334.
42 I. Levchuk, A. Osvet, X. Tang, M. Brandl, J. D. Perea, F. Hoegl, G. J. Matt, R. Hock, M. Batentschuk and C. J. Brabec, *Nano Lett.*, 2017, **17**, 2765–2770.
43 M. C. Weidman, M. Seitz, S. D. Stranks and W. A. Tisdale, *ACS Nano*, 2016, **10**, 7830–7839.
44 J. C. Blancon, H. Tsai, W. Nie, C. C. Stoumpos, L. Pedesseau, C. Katan, M. Kepenekian, C. M. M. Soe, K. Appavoo, M. Y. Sfeir, S. Tretiak, P. M. Ajayan, M. G. Kanatzidis, J. Even, J. J. Crochet and A. D. Mohite, *Science*, 2017, **355**, 1288–1292.
45 L. Protesescu, S. Yakunin, S. Kumar, J. Bär, F. Bertolotti, N. Masciocchi, A. Guagliardi, M. Grotevent, I. Shorubalko, M. I. Bodnarchuk, C.-J. Shih and M. V. Kovalenko, *ACS Nano*, 2017, **11**, 3119–3134.
46 C. Liang, D. Zhao, Y. Li, X. Li, S. Peng, G. Shao and G. Xing, *Energy Environ. Mater.*, 2018, **1**, 221–231.
47 S. Adjokatse, S. Kahmann, H. Duim and M. A. Loi, *APL Mater.*, 2019, **7**, 031116.

48 C. F. J. Lau, M. Zhang, X. Deng, J. Zheng, J. Bing, Q. Ma, J. Kim, L. Hu, M. A. Green, S. Huang and A. Ho-Baillie, *ACS Energy Lett.*, 2017, **2**, 2319–2325.
49 L. Martínez-Sarti, S. H. Jo, Y.-H. Kim, M. Sessolo, F. Palazon, T.-W. Lee and H. J. Bolink, *Nanoscale*, 2019, **11**, 12793–12797.
50 X. Zhang, C. Wang, Y. Zhang, X. Zhang, S. Wang, M. Lu, H. Cui, S. V. Kershaw, W. W. Yu and A. L. Rogach, *ACS Energy Lett.*, 2018, **4**, 242–248.
51 D. H. Cao, C. C. Stoumpos, O. K. Farha, J. T. Hupp and M. G. Kanatzidis, *J. Am. Chem. Soc.*, 2015, **137**, 7843–7850.
52 P. Caprioglio, F. Zu, C. M. Wolff, J. A. Márquez Prieto, M. Stolterfoht, P. Becker, N. Koch, T. Unold, B. Rech, S. Albrecht and D. Neher, *Sustainable Energy Fuels*, 2019, **3**, 550–563.
53 K. Chen, Q. Zhong, W. Chen, B. Sang, Y. Wang, T. Yang, Y. Liu, Y. Zhang and H. Zhang, *Adv. Funct. Mater.*, 2019, **29**, 1900991.
54 A. Walsh, D. O. Scanlon, S. Chen, X. G. Gong and S.-H. Wei, *Angew. Chem., Int. Ed.*, 2015, **54**, 1791–1794.
55 R. Grisorio, E. Fanizza, I. Allegretta, D. Altamura, M. Striccoli, R. Terzano, C. Giannini, V. Vergaro, G. Ciccarella, N. Margiotta and G. P. Suranna, *Nanoscale*, 2020, **12**, 623–637.
56 J. De Roo, M. Ibáñez, P. Geiregat, G. Nedelcu, W. Walravens, J. Maes, J. C. Martins, I. Van Driessche, M. V. Kovalenko and Z. Hens, *ACS Nano*, 2016, **10**, 2071–2081.
57 G. Almeida, L. Goldoni, Q. Akkerman, Z. Dang, A. H. Khan, S. Marras, I. Moreels and L. Manna, *ACS Nano*, 2018, **12**, 1704–1711.
58 E. Hassanabadi, M. Latifi, A. F. Gualdrón-Reyes, S. Masi, S. Y. joon, M. Poyatos, B. Julián-López and I. Mora Seró, *Nanoscale*, 2020, **12**, 14194–14203.
59 V. K. Ravi, R. A. Scheidt, A. Nag, M. Kuno and P. V. Kamat, *ACS Energy Lett.*, 2018, **3**, 1049–1055.
60 V. S. Chirvony, K. S. Sekerbayev, H. Pashaei Adl, I. Suárez, Y. T. Taurbayev, A. F. Gualdrón-Reyes, I. Mora-Seró and J. P. Martínez-Pastor, *J. Lumin.*, 2020, **221**, 117092.
61 M. Anaya, J. F. Galisteo-López, M. E. Calvo, J. P. Espinós and H. Míguez, *J. Phys. Chem. Lett.*, 2018, **9**, 3891–3896.
62 R. Zhu, Z. Luo, H. Chen, Y. Dong and S.-T. Wu, *Opt. Express*, 2015, **23**, 23680.

